Maximum Power Point Tracking Converter Based on the Open-Circuit Voltage Method for Thermoelectric Generators

Andrea Montecucco, *Student Member, IEEE*, and Andrew R. Knox, *Senior Member, IEEE*

***Abstract*—Thermoelectric generators (TEGs) convert heat energy into electricity in a quantity dependent on the temperature difference across them and the electrical load applied. It is critical to track the optimum electrical operating point through the use of power electronic converters controlled by a maximum power point tracking (MPPT) algorithm. The MPPT method based on the open-circuit voltage is arguably the most suitable for the linear electrical characteristic of TEGs. This paper presents an innovative way to perform the open-circuit voltage measure during the pseudonormal operation of the interfacing power electronic converter. The proposed MPPT technique is supported by theoretical analysis and used to control a synchronous Buck–Boost converter. The prototype MPPT converter is controlled by an inexpensive microcontroller, and a lead-acid battery is used to accumulate the harvested energy. Experimental results using commercial TEG devices prove that the converter accurately tracks the maximum power point during thermal transients. Precise measurements in the steady state show that the converter finds the maximum power point with a tracking efficiency of 99.85%.**

***Index Terms*—Buck-Boost, converter, dc–dc, maximum power point tracking (MPPT), synchronous, thermoelectric (TE), thermoelectric generator (TEG).**

I. Introduction

THERMOELECTRIC generators (TEGs) are physically and electrically robust semiconductor devices able to convert thermal energy into electrical energy, provided that a temperature gradient is maintained across them, exploiting the Seebeck effect [1]. In the steady state, they can be modeled by a dc voltage source in series with an internal resistance, therefore for the theorem of maximum power (MP) transfer if the load matches the internal resistance then MP is produced. A description of the structure and functioning of a typical thermoelectric (TE) device is presented in Section II-A.

Due to relatively high cost and low efficiency—around 5%—the use of TEGs has been in the past restricted to specialized medical, military, remote, and space applications [2]. However, in recent years, an increasing environmental issues and energy cost have motivated research into alternative commercial methods of generating electrical power. TEs is one of several that has emerged as a viable source of electricity [3]. Moreover, the efficiency of TEGs is improving [4], [5] and the device cost is decreasing. Consequently, TEGs can now be successfully employed to harvest the heat energy rejected by other processes (automotive [6], [7], stove [8]–[11], geothermal [12], or power stations [13], [14]), to power sensors [15]–[18] or to increase the system efficiency in symbiotic applications [20]. Mass-produced energy scavenging applications such as exhaust gas systems are likely to lead to a further reduction of TE device cost [21]. In applications of waste heat harvesting, the input thermal power is essentially free; therefore the low conversion efficiency is not a serious drawback *per se*, but it is important to maximize the power obtained from the device utilized in order to minimize the cost per Watt produced.

The magnitude of the TEG's open-circuit voltage is directly proportional to the temperature difference, and like with solar cells a convenient number of TEGs can be connected in series or parallel in order to achieve desired levels of voltage and current. Power electronic converters are very often used to interface TEGs to the required load. The choice of converter typology depends on the output and input voltages; as an example, for connection to dc microgrids a high step-up gain converter is required [22], while for connection to a 12-V car battery a Buck or Buck–Boost type can be used. This work uses a synchronous Buck-Boost to guarantee a wide input voltage range and consequently harvest power from the TEGs over a wide range of operating temperatures.

TEGs are often employed in dynamic environments with time-varying temperature differences, e.g., cars' exhaust gas systems [19], [23], therefore it is of great importance to quickly and precisely adjust the best electrical operating point in order to always maximize the harvested power. It is necessary to control the power electronic converters with a maximum power point tracking (MPPT) algorithm that matches the virtual load seen by the TEG to its actual internal resistance by changing the duty cycle of the converter. Ideally, each TEG should be independently electronically controlled but this would greatly increase the number of MPPT power electronic converters needed and adversely affect the cost of implementing the system. As a consequence, TEGs are often electrically interconnected in series and/or parallel to form arrays [24]. This leads to the formation of what is called a distributed MPPT (DMPPT) subsystem in which each TEG array's electrical operating point is controlled

Manuscript received 16 Dec. 2013; revised 4 Feb. 2014; accepted 10 Mar. 2014. Date of publication March 21, 2014; date of current version October 7, 2014. This work was supported by the Engineering and Physical Sciences Research Council under Grant EP/K022156/1 (RCUK). Recommended for publication by Associate Editor M. Vitelli.

The authors are with the School of Engineering, University of Glasgow, Glasgow G12 8LT, U.K. (e-mail: andrea.montecucco@glasgow.ac.uk; andrew.knox@glasgow.ac.uk).

Color versions of one or more of the figures in this paper are available online at http://ieeexplore.ieee.org.

Digital Object Identifier 10.1109/TPEL.2014.2313294

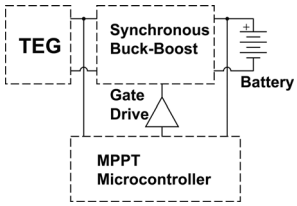

Fig. 1. Blocks diagram illustrating the fundamental structure of the proposed system.

independently in a similar way as for photovoltaics (PV) systems [25]. An additional centralized MPPT function could be required if an inverter is employed for grid connection, thus forming an hybrid MPPT system [26].

In the literature, the most used MPPT algorithms for TEGs are the Perturb & Observe (P&O) [27]–[29] and the incremental conductance (INC) [30]. These MPPT algorithms have originally been developed for PV systems, in which the relationship between voltage and current is logarithmic. On the contrary, in TEGs, the electrical characteristic is linear:

$$V_{\mathrm{MP}} = \frac{V_{\mathrm{OC}}}{2} \quad \text{and} \quad I_{\mathrm{MP}} = \frac{I_{\mathrm{SC}}}{2} \tag{1}$$

where V_{MP} and I_{MP} are the voltage and current at the maximum power point, V_{OC} is the open-circuit voltage and I_{SC} is the short-circuit current. MPPT algorithms that use this relationship either measure the open-circuit voltage [17], [31], [32] or the short-circuit current [22]; they provide a number of advantages over the aforementioned methods:

1) measurement of only one parameter (voltage or current);
2) lower numerical computational requirements;
3) no steady-state oscillation (P&O) or error (INC).

These methods have the disadvantage that no energy flows from the TEG to the converter during the sampling time because the converter must be disconnected from the TEG to allow for the measurement of V_{OC} or I_{SC}. In the literature, Laird *et al.* [33] compared P%O, INC, and fractional I_{SC}.

This paper proposes an innovative open-circuit voltage measurement technique, described and analyzed in Section III, that can be undertaken during the normal switching of the converter, with a minimal reduction in collection efficiency.

Fig. 1 shows the block diagram of the proposed system, where the TEG array is connected to the input of a synchronous noninverting Buck–Boost converter, which is described in Section IV. A microcontroller implements the MPPT algorithm controlling the transfer of energy from the TEGs and driving the converter MOSFET switches through gate drivers. The load is represented by a battery.

The proposed MPPT prototype converter is tested with real TEGs, both in steady state and under thermal transients; the experimental results are presented in Section V, before drawing the conclusions.

II. TE Power Generating System

This Section first describes the structure and functioning of a typical TE device; second, it presents the test rig used in the experiments and finally the performance of the TEGs used in the experiments is analyzed.

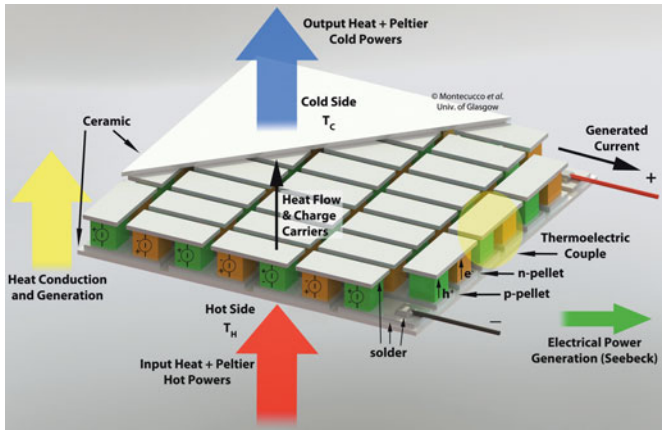

Fig. 2. Mechanical drawing illustrating the components of a TE device and the physical phenomena happening during power generation.

A. TE Power Generating Device

A TE device is composed of n- and p-doped semiconductor pellets electrically connected in series and thermally in parallel. In the power generation mode, every pellet produces a voltage differential when a temperature gradient ΔT is established at its sides, thanks to the Seebeck effect [1]; the voltage magnitude is linearly dependent on ΔT and the Seebeck coefficient α, which is a property of the material used and varies with temperature. As shown in Fig. 2, each voltage adds up thanks to the series connection and when a load is connected to the TEG's terminals, current flows through the device, because both electrons and holes are moved from the hot to the cold side by the flow of heat. This current flow produces heat by Joule heating and pumps additional heat from the hot to the cold side because of the Peltier effect, which is considered a parasitic effect in power generation; in fact it effectively increases the thermal conductivity of the device. A high load current amplifies the Peltier effect, which increases the effective thermal conductivity of the device which in turns decreases the temperature difference ΔT [34].

In the steady state, a TEG can effectively be modeled by a voltage source V_{OC} in series with an internal resistance R_{int} [35], [36], which slightly varies with the average temperature of the TEG, affecting the slope of the *V–I* curve.

The cross-sectional area of the pellets greatly influences the internal resistance and the current–voltage rating of the device. A module with wide pellets can fit a small number of pellets, therefore it will have relatively small output voltage and internal resistance, but high output current [37]. As an example, Table I shows how the size and number of pellets influences the current–voltage ratings in two TEGs offered by European Thermodynamics Ltd.

The most commonly used material is Bismuth Telluride (Bi_2Te_3), however other materials like *Silicides, Skutterudites, Oxysulphides, Ti–S, Ni–Cr–S,* and *Cobalt* oxides are being developed for automotive applications over a range of temperatures [38]–[41]. These materials have a variety of issues (e.g.,

TABLE I
COMPARISON OF SOME GEOMETRICAL AND ELECTRICAL PARAMETERS BETWEEN TWO TEG DEVICES OFFERED BY EUROPEAN THERMODYNAMICS LTD

Product Code	Pellet Area (mm^2)	Pellet Number	Electrical V_{OC} (V)	Electrical I_{SC} (A)	Electrical R_{int} (Ω)
GM250-449-10-12	1	898	17	1	16.5
TEHP1-12656-0.2	6.25	252	2.7	7.5	0.35

Both TEGs have a surface area of 3136 mm^2. The electrical parameters are measured at ΔT = 100°C.

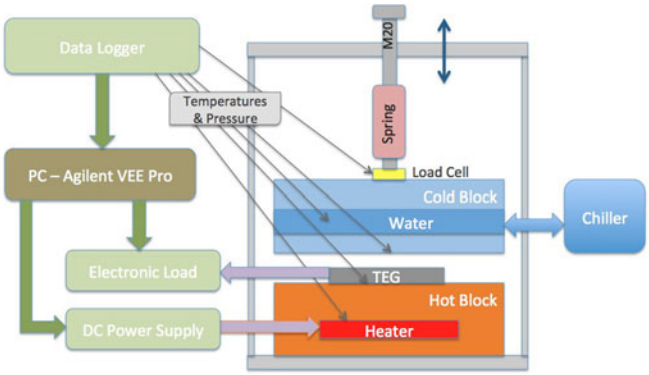

Fig. 3. Schematic of the mechanical test rig used in the experiments.

they are difficult to form electrical connections to, they are chemically reactive at high temperatures and expensive to manufacture) which still have to be overcome before their large-scale commercial deployment is viable.

B. Mechanical Test Rig

The test rig used in this work is designed to test TEG performance providing accurate repeatable measurements. A complete description of the system can be found in [42]. This test apparatus is able to independently control the mechanical load and the temperature difference across each of the four TEG channels that can be used at the same time. Fig. 3 illustrates the schematic of one channel. The TEG device is sandwiched between a hot block and a cold block. The former contains a high-temperature high-power heater powered by a dc power supply, while the latter is water-cooled by a chiller unit. The output of the TEG can be connected to an electronic load or to any other desired load. A load cell measures the mechanical pressure over the TEG and thermocouple sensors are fitted through the copper blocks touching the TEGs' hot and cold faces, in order to obtain precise temperature measurements. *Agilent* VEE Pro is a graphical programming tool for automated control of the laboratory equipment. A VEE Pro program operates all the instruments and precisely controls the temperature difference across the TE devices to the desired value. Using such equipment, it is possible to do an accurate electrical characterization of the TEG under test, sweeping the load at different values, all at the same temperature difference.

C. TEGs' Electrical Characteristic

In the experiments presented in Section V of this paper, three TEG devices from European Thermodynamics Ltd. (product code GM250-127-14-10) have been used. Each one was characterized separately at three different temperature gradients ΔT: 100 °C, 150 °C, and 200 °C. Every test was performed imposing 1.25 MPa of mechanical pressure onto each TEG, which corresponds to 209 kg on a surface of $40 \times 40\,\mathrm{mm}^2$. Fig. 4 plots the output voltage and power versus current for one of the TEGs (TEG#2).

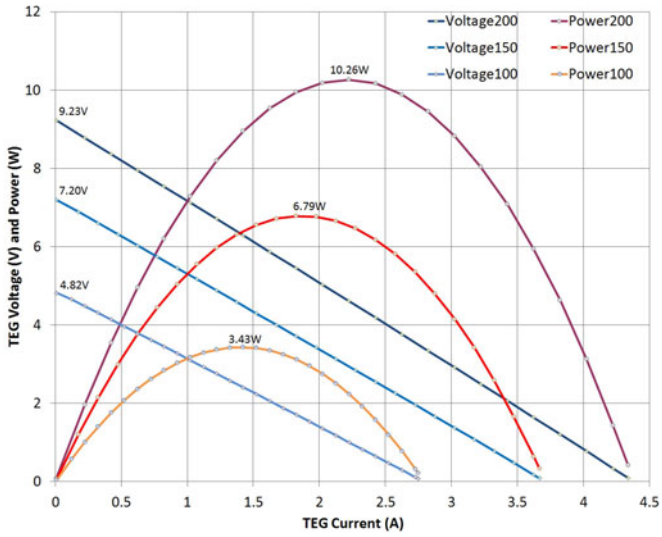

Fig. 4. Experimental electrical characterization for the TEG module # 2. The gray dots in the curves represent experimental data points. $\Delta T = 100\,^{\circ}\mathrm{C}, 150\,^{\circ}\mathrm{C}, 200\,^{\circ}\mathrm{C}$, clamped at $2\,\mathrm{kN}/1.25\,\mathrm{MPa}$.

Table II lists the performance data of the three TEGs. The maximum deviation in performance between the three devices stands at less than 5% for power production; this difference may be due to manufacturing tolerances, contact resistance mismatch, or measurement accuracy. However, this performance variation will not influence the MPPT converter evaluation, as it will be explained shortly. These data are used to formulate a mathematical characterization using a similar technique to that explained in [43]. Voltage and power are calculated as a function of the current load and temperature difference.

In the steady state, it can be written that

$$V_{\mathrm{load}} = V_{\mathrm{OC}} - R_{\mathrm{int}} I_{\mathrm{load}}. \tag{2}$$

The open-circuit voltage is proportional to the Seebeck coefficient α ($V_{\mathrm{OC}} = \alpha \Delta T$), which varies depending on the Thomson coefficient [44]. A 2nd-order polynomial fitting technique has been used to model the variation of V_{OC} and R_{int} with ΔT. Using a similar technique to [43], (2) can now be written as

$$V_{\mathrm{load}} = (a\Delta T^2 + b\Delta T + c) - (d\Delta T^2 + e\Delta T + f) I_{\mathrm{load}} \tag{3}$$

where a, b, c, d, e, and f are constant coefficients, different for each TEG, obtained from the experimental data. Even if the performance variation for the three devices used is up to 5%, the actual expected performance is calculated for each TEG individually.

Using (3), it is possible to replicate the electrical characteristics of the TEGs used, after obtaining the necessary parameters from the experimental data. Fig. 5 shows the resulting

TABLE II
PERFORMANCE PARAMETERS FOR THE THREE TE MODULES USED IN THE EXPERIMENT

	$TEG\#1$			$TEG\#2$			$TEG\#3$			Deviation		
ΔT ($^\circ C$)	R_{int} (Ω)	V_{OC} (V)	P_{max} (W)	R_{int} (Ω)	V_{OC} (V)	P_{max} (W)	R_{int} (Ω)	V_{OC} (V)	P_{max} (W)	R_{int} (%)	V_{OC} (%)	P_{max} (%)
100	1.73	4.84	3.43	1.73	4.87	3.44	1.80	4.87	3.33	3.8	0.7	3.2
150	1.94	7.22	6.79	1.94	7.23	6.80	2.01	7.21	6.57	3.6	0.2	3.4
200	2.11	9.25	10.26	2.10	9.25	10.30	2.17	9.20	9.84	3.3	0.5	4.5

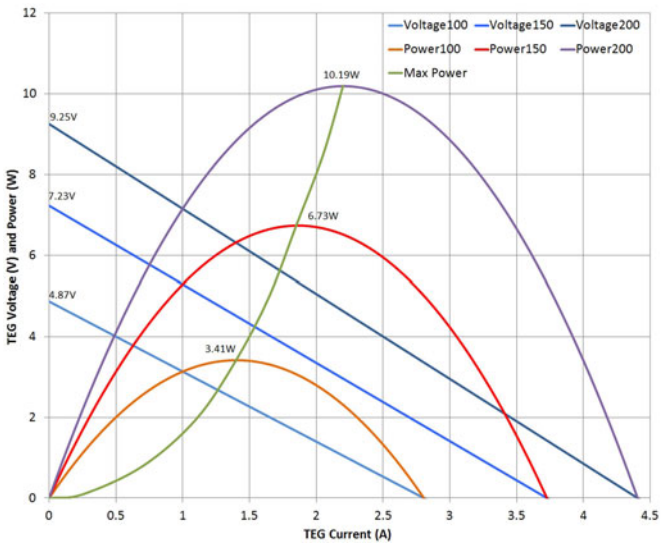

Fig. 5. "Mathematical" electrical characterization for the TEG module # 2.

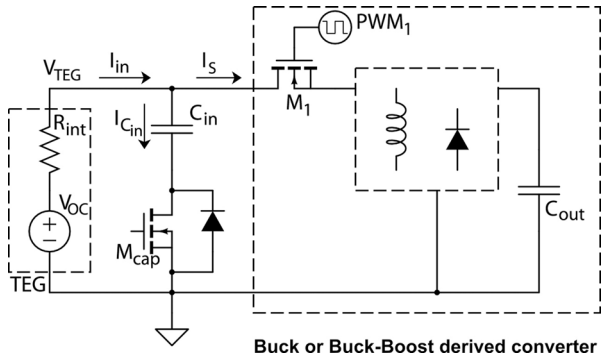

Fig. 6. Schematic drawing of the components required for the proposed MPPT technique.

"mathematical" electrical characterization for TEG# 2. As it can also be appreciated from a comparison with Fig. 4, the average deviation between the mathematically derived values and the experimental data is always less than 1.5%. This means that it is now possible to independently predict the output from each of the three TEGs at any temperature difference with high confidence, even when they are at different thermal operating points. This formulation is used to compare the performance of the MPPT converter in Section V.

III. MPPT METHOD

It was explained in Section I that the method usually called *(fractional) open-circuit voltage* consists in measuring the TEG's open-circuit voltage and then setting the *at-load* operating voltage at half of $V_{\rm OC}$. This method normally requires the converter to be disconnected for a certain duration to allow for the converter's input capacitors to be charged up to $V_{\rm OC}$ [33]; during such time no power is harvested. In order to meet the RMS input current requirements, input capacitors might be in the order of tens of microfarad, which means that they may need hundreds of microsecond to charge up to $V_{\rm OC}$, depending on $R_{\rm int}$. Sometimes, an additional series switch is needed to disconnect the TEGs from the converter [17], [32]. This switch might need a high-side gate driver with continuous conduction time for long periods. This switch introduces additional I^2R losses when it is closed, and its use interrupts the normal operation of the converter, thus creating a transient event every time the $V_{\rm OC}$ measurement is taken. The method that we have already presented at ECCE'12 [45] reduces these drawbacks. Following is a description of this method and a theoretical analysis of its performance.

A. Open-circuit Voltage MPPT Method

This section describes an innovative technique to measure the open-circuit voltage of a TEG, which can be used with any converter topology derived from the Buck or Buck-Boost having a switch at its input. The basic circuit schematic, which highlights the necessary components required, is provided in Fig. 6. A TEG is connected to the input of a Buck or Buck–Boost derived converter. The converter's input capacitors $C_{\rm in}$ are connected to ground through the switch $M_{\rm cap}$. The high-side switch M_1 represents the input switch of a Buck or Buck–Boost converter, while the remaining converter's components are generically represented by the following box connected to the output capacitors $C_{\rm out}$.

To aid explanation of how the voltage measurement is achieved, a timing diagram for the operation of the aforementioned switches is provided in Fig. 7. In the next description, $t_{\rm on}$ and $t_{\rm off}$ are the high and low states of pulse width modulation ($\rm PWM_1$), respectively. Under normal operation, $M_{\rm cap}$ is closed and $C_{\rm in}$ contributes to the pulsating input current required by the converter during $t_{\rm on}$. When the open-circuit voltage measurement is required, $M_{\rm cap}$ gets opened. The bottom part of Fig. 7 provides a zoomed-in view of what happens in this situation. During $t_{\rm off}$, M_1 is open and the TEG is momentarily disconnected from the converter. The current cannot flow into $C_{\rm in}$, hence the potential at the TEG's terminals rises to the open-circuit voltage $V_{\rm OC}$, typically within tens of nanoseconds [27]. The microcontroller is timed to measure $V_{\rm TEG}$ during $t_{\rm off}$ while the converter is still operating in a pseudonormal state: as it will be analyzed in the next section, both the TEG and $C_{\rm in}$ are still providing power to the converter during $t_{\rm on}$. The open-circuit measurement process is repeated every $T_{\rm meas}$, which is a design

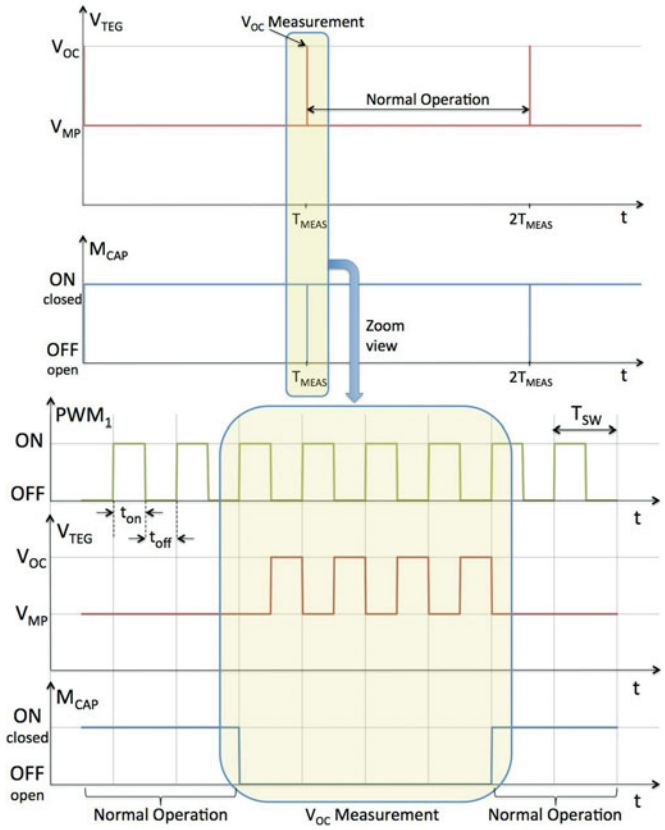

Fig. 7. Timing diagram explaining how the open-circuit voltage measurement is achieved. The bottom part of the image provides a zoomed-in view of the measurement operation, which takes place every T_{meas}.

parameter that depends on the thermal time constant of the TEG system used. It is usually chosen based on experience and it is typically between 0.1 and 1 s. In between V_{OC} measurements, a digital control loop keeps on adjusting the converter's duty cycle to maintain V_{TEG} at half of V_{OC}.

This V_{OC} measurement technique is considerably faster than disconnecting the converter (by keeping PWM_1 low) until C_{in} reaches V_{OC}. Also, it is more accurate because when the TEG is kept at open circuit the Peltier effect is null, therefore the temperature difference increases slightly, and with it V_{OC}, leading to a wrong V_{OC} value [46]; this means that the converter would choose a slightly higher operating voltage. On the contrary, such problem does not occur using the proposed MPPT method because the TEG is left at the open circuit for less than a switching period.

B. Theoretical Analysis of MPPT Efficiency

This section presents a theoretical analysis to quantify the losses introduced by the additional switch M_{cap} in series with C_{in}, and by the V_{OC} measurement technique used. In order to do so, it is necessary to calculate the RMS current $I_{C_{\mathrm{in}_{\mathrm{RMS}}}}$ flowing into the input capacitors and to understand the converter's behavior in response to the measurement technique.

Without loss of accuracy, we can consider either a Buck or Buck–Boost converter for what concerns the input capacitors' RMS current calculations.

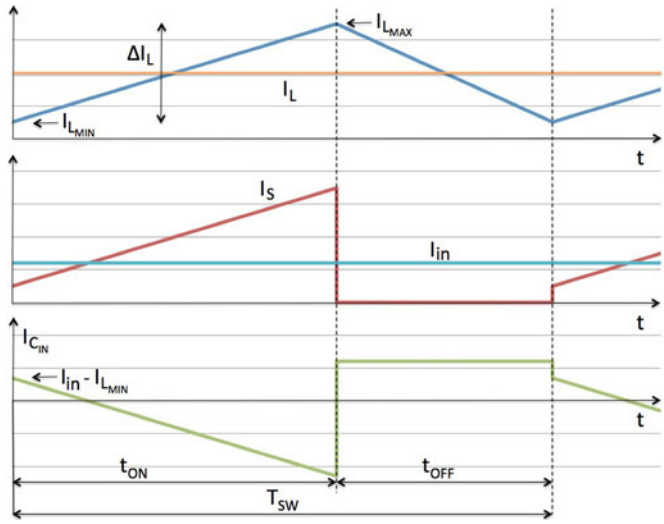

Fig. 8. Plots of the currents in a Buck or Buck-Boost derived converter without M_{cap} (values are generic): in the inductor (I_L blue, and $I_{L_{\mathrm{AVG}}}$ orange); in the switch (I_S red) and average input current (I_{in} light blue); in the input capacitor ($I_{C_{\mathrm{in}}}$ green).

The input capacitors are important because they store additional energy from the input source when the switch M_1 is open during the off-time t_{off} of the switching period T_{sw}, and provide it to the load when M_1 closes. The input current is pulsating, and the amount of current that the input source can provide is limited by its series resistance, which is usually fairly high (one half to several ohms) in TEGs.

Referring to the plots in Fig. 8, the current I_S (in red) flows in the converter's switch only during the on-time t_{on} of the switching period T_{sw}, while it stays at zero for the rest of T_{sw}. During t_{off}, the input source charges C_{in}, which effectively filters an ac current. The input current I_{in} (in light blue) can be written as $I_S + I_{C_{\mathrm{in}}}$ or as the average of I_S over T_{sw}.

Let us assume that the MPPT converter is setting the correct MP point at the TEG's output, so that the average input capacitor's voltage is $V_{\mathrm{MP}} = V_{\mathrm{OC}}/2$. Considering a small voltage ripple on C_{in} [47], during t_{off}, C_{in} is charged by the current $I_{C_{\mathrm{in,off}}} = V_{\mathrm{OC}}/2R$, in which $R = R_{\mathrm{int}} + \mathrm{ESR}$, sum of the TEG's internal resistance and the equivalent series resistance (ESR) of the input capacitors. We can calculate the RMS of $I_{C_{\mathrm{in,off}}}$ as

$$I^2_{C_{\mathrm{in,off}_{\mathrm{RMS}}}} = D' I^2_{\mathrm{in}} = \frac{D' V^2_{\mathrm{OC}}}{4R^2} \tag{4}$$

where D is the duty cycle of the converter and $D' = (1 - D)$.

For the trapezoidal segment of $i_{C_{\mathrm{in}}}(t)$ during t_{on}, the RMS current into C_{in} is

$$I^2_{C_{\mathrm{in,on}_{\mathrm{RMS}}}} = \frac{D}{3}\Big[(I_{\mathrm{in}} - I_{L_{\mathrm{min}}})^2 + (I_{\mathrm{in}} - I_{L_{\mathrm{max}}})^2 + \\ + (I_{\mathrm{in}} - I_{L_{\mathrm{min}}})(I_{\mathrm{in}} - I_{L_{\mathrm{max}}}) \Big]. \tag{5}$$

For both Buck and Buck–Boost converters $I_L = I_{\mathrm{in}}/D$; therefore, we can write that $I_{\mathrm{in}} - I_L = I_{\mathrm{in}}(1 - 1/D) = -D' I_{\mathrm{in}}/D$. Also, $I_{L_{\mathrm{min}}} = I_L - \Delta I_L/2$ and $I_{L_{\mathrm{max}}} = I_L + \Delta I_L/2$. Using

these relationships in (5) and knowing that for both Buck and Buck–Boost converters $\Delta I_L = \frac{V_{\rm out} D'}{f_{\rm sw} L}$, we obtain

$$I^2_{C_{\rm in,on_{RMS}}} = D'^2 \left[\frac{I^2_{\rm in}}{D} + \frac{D V^2_{\rm out}}{12 f^2_{\rm sw} L^2} \right] \tag{6}$$

where $i_{C_{\rm in}}(t)$ is a periodic waveform composed of two orthogonal piecewise segments [48], therefore its RMS value can be obtained from (4) and (6):

$$I_{C_{\rm in_{RMS}}} = \sqrt{D' \left[\frac{I^2_{\rm in}}{D} + \frac{D D' V^2_{\rm out}}{12 f^2_{\rm sw} L^2} \right]}. \tag{7}$$

The power dissipated on the low-side switch $M_{\rm cap}$ in series with the input capacitors is

$$P_{M_{\rm cap}} = r_{\rm on} I^2_{C_{\rm in_{RMS}}} \tag{8}$$

where $r_{\rm on}$ is the on-resistance of the switch used. Section IV-B provides the losses value for the converter used. The switching and body diode losses of $M_{\rm cap}$ are almost irrelevant because they occur for a few microsecond every $T_{\rm meas}$.

Referring to Figs. 6 and 8, let us now consider what happens when $M_{\rm cap}$ is switched open. In this case, the TEGs can supply power to the converter only during $t_{\rm on}$, because during $t_{\rm off}$ M_1 is open and current cannot flow into $C_{\rm in}$, hence the TEGs go to the open circuit. During $t_{\rm on}$, the internal resistance $R_{\rm int}$ limits the quantity of current that can flow from the TEGs, and the body diode of $M_{\rm cap}$ is forced into conduction so that $C_{\rm in}$ supplements the additional current required by the converter and slightly discharge.

After each PWM period $T_{\rm sw}$, the voltage across $C_{\rm in}$ decreases because when $M_{\rm cap}$ is open the input capacitor cannot be charged as it would normally happen during $t_{\rm off}$. Provided that $M_{\rm cap}$ is left open for just a few cycles, the capacitance of $C_{\rm in}$ is usually enough to guarantee that $v_{\rm in}(t)$ does not decrease significantly; the following calculations are useful to estimate how much the voltage on the capacitor sags during the $V_{\rm OC}$ measurement. The initial energy stored in $C_{\rm in}$ is $E_{C_{\rm in}0} = C_{\rm in} V^2_{C_{\rm in}0}/2$. To derive the worst-case scenario, let us consider that $I_{L_{\rm min}} - I_{\rm in} \geq 0$ and let us calculate the energy removed from $C_{\rm in}$ during the $t_{\rm on}$ of one switching cycle:

$$\begin{aligned} E_{1_{\rm PWM}} &= \int_0^{t_{\rm on}} v_{C_{\rm in}(t)} i_{C_{\rm in}(t)}\, dt \\ &= \int_0^{t_{\rm on}} \left(I_{L_{\rm min}} - I_{\rm in} + \Delta I_L \frac{t}{t_{\rm on}} \right) V_{\rm in}\, dt \\ &= V_{\rm in} D T_{\rm sw} (1-D) I_L = P_{\rm in} D' T_{\rm sw} \end{aligned} \tag{9}$$

where we considered $v_{\rm in}(t)$ constant at $V_{\rm in}$. This slightly overestimates the calculation of the voltage drop because after every $T_{\rm sw}$ $v_{\rm in}(t)$ decreases.

The final energy stored in $C_{\rm in}$ is

$$E_{C_{\rm in}f} = E_{C_{\rm in}0} - n_{\rm PWM} E_{1_{\rm PWM}} = \frac{1}{2} C_{\rm in} V^2_{C_{\rm in}f} \tag{10}$$

where $n_{\rm PWM}$ is the number of PWM cycles elapsed with $M_{\rm cap}$ open. From (10), it is possible to obtain $V_{C_{\rm in}f}$, which is the voltage on $C_{\rm in}$ at the end of the $V_{\rm OC}$ measurement procedure.

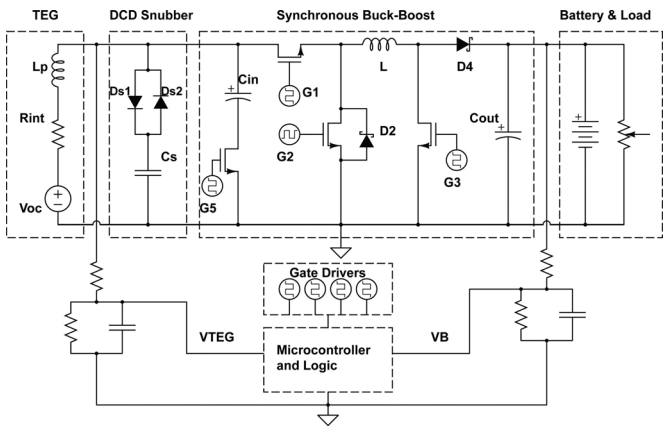

Fig. 9. Schematic of the complete system proposed.

IV. MPPT Converter

This section presents the noninverting synchronous Buck–Boost dc–dc converter, whose schematic diagram of the complete system is shown in Fig. 9. A generic TEG is represented by a voltage source $V_{\rm OC}$, an internal resistance $R_{\rm int}$, and a parasitic inductance L_p. An innovative snubber, described in the Section IV-A, is connected across the input of the synchronous Buck–Boost converter to suppress overvoltage transients. The converter supplies power to a battery and to an auxiliary electronic load. A microcontroller, measuring the input and output voltages, computes the MPPT algorithm and controls the gate drivers of the converter's MOSFETs. The power stage is described in Section IV-B.

A. Overvoltage Snubber

When a TEG is suddenly disconnected from the load, it goes to the open circuit after a very fast underdamped oscillation with frequency usually in the order of megahertz [27]. This is due to the fact that a parasitic inductance L_P is built up in the many solder connections between pellets in the TEG, in the cables from the TE device to its load, and in the printed-circuit board (PCB)'s tracks. Such parasitic inductance forms a resonating tank with the parasitic capacitances of the circuit and it is damped by the TEG's internal resistance $R_{\rm int}$.

In the circuit of Fig. 6, when $M_{\rm cap}$ is closed and M_1 opens at the beginning of $t_{\rm off}$, $I_{\rm in}$ finds an alternative path into $C_{\rm in}$, which is a fairly big capacitance. This cannot happen when $M_{\rm cap}$ is open, hence the TEG is suddenly open-circuited. The current in L_p cannot stop flowing instantaneously and its energy is dissipated in the ringing with the parasitic capacitances of the circuit, damped by $R_{\rm int}$, i.e., an *RLC* circuit. The decrease of $I_{\rm in}$ reverses the voltage across the parasitic inductance, so that a voltage considerably greater than $V_{\rm OC}$ appears at the converter's input.

Fig. 10 shows an experimental switching transient test undertaken on one of the TEG modules used. At the beginning of the transient, t_0, the voltage sharply rises from the operating voltage $V_{\rm load}$ to $V_{\rm max}$; this increases the switching transition losses on M_1 and it also requires M_1 to have a higher

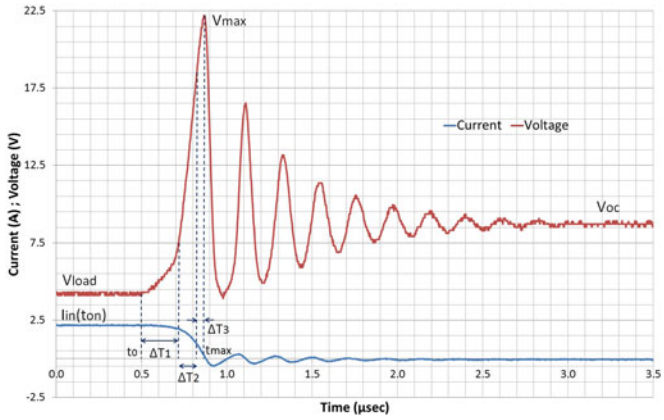

Fig. 10. TEG's voltage and current during a switching transient from at-load operation to open circuit.

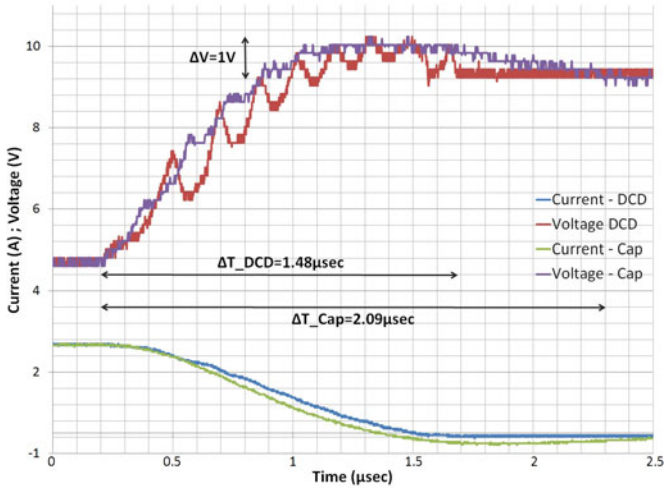

Fig. 11. Experimental comparison of TEG's voltage and current during a switching transient from at-load operation to open circuit, when using a damping capacitor only or with the proposed DCD snubber.

maximum drain–source voltage rating. Due to the *RLC* oscillatory nature, when $V_{\rm TEG}$ reaches $V_{\rm max}$ the inductor current (in blue in Fig. 10) reverses and flows into the TEG; the Peltier effect is reversed and the Joule heating is of similar magnitude, therefore it is not a problem for the TEG. The maximum voltage that can be applied to a TE device in Peltier cooling mode is higher than $V_{\rm OC}$ and a TEG can stand high levels of Joule heating; also, TE devices do not contain voltage insulating layers or other materials susceptible to voltage stress.

L_P can be approximately calculated from Fig. 10. At the end of $t_{\rm on}$, the current $I_{\rm in}(t_{\rm on})$ flows through L_P. In order to avoid ambiguity in the equations, $I_{\rm in}(t_{\rm on})$ will be written $I_{\rm in}, t_{\rm on}$. The energy contained into L_P is

$$E_{L_P} = \frac{1}{2} L_P I^2_{\rm in,t_{on}}. \tag{11}$$

This energy is completely transferred to the parasitic capacitance when $V_{\rm TEG} = V_{\rm max}$ and $I_{\rm in} = 0$. The basic inductor relationship $v_L(t) = L\frac{di(t)}{dt}$ can be approximated for L_P to

$$V_{\rm max} - V_{\rm load} = L_P \frac{I_{\rm in,t_{on}}}{t_{\rm max} - t_0} \tag{12}$$

where $t_{\rm max}$ is the time at which $V_{\rm TEG} = V_{\rm max}$. L_P can be calculated from (12) using the values obtained from the waveforms of Fig. 10. However, it should be noted that the rise of $V_{\rm TEG}$ to $V_{\rm OC}$ is not linear. The linear region is approximately between 20% and 80% of the increase. Dividing $\Delta T = t_{\rm max} - t_0$ in three intervals where the middle interval ΔT_2 corresponds to the linear region, we can see that $\Delta T_2 \approx (\Delta T_1 + \Delta T_3)/4$. As a consequence, we can apply a "correction factor" to the calculated value for L_P, which now becomes

$$L_P = \frac{\Delta T(V_{\rm max} - V_{\rm load})}{4 I_{\rm in,t_{on}}}. \tag{13}$$

In order to damp the overvoltage, while still achieving a fast transient of the TEG's voltage to the open circuit, a capacitor C_S is added across the TEG's terminals. C_S needs to be sufficiently large so that the energy transferred from L_P does not charge it to much more than $V_{\rm OC}$, but small enough to let $V_{\rm TEG}$ quickly settle to $V_{\rm OC}$. The value of such capacitor can be chosen using the energy calculated in (11). Before the transient C_S is already charged at $V_{\rm load}$, with a stored energy $1/2 C_S V^2_{\rm load}$. If we want all the energy in L_P to be transferred to C_S when it reaches $V_{\rm OC}$, then the energy balance states that

$$\frac{1}{2} L_P I^2_{\rm in,t_{on}} = \frac{1}{2} C_S \left(V^2_{\rm OC} - V^2_{\rm load}\right). \tag{14}$$

When working at MP point $V_{\rm OC} = 2V_{\rm load}$, therefore (14) leads to $C_S = L_P/3R^2_{\rm int}$. However, given the wide range of $V_{\rm load}$ (depending on the temperature difference), the choice of C_S is by necessity a compromise. Our experiments have shown the following solution to be the most satisfactory:

$$C_S = \frac{L_P}{R^2_{\rm int}} \tag{15}$$

which corresponds to removing the dc offset $V_{\rm load}$ in C_S from (14), which becomes $L_P I^2_{\rm in,t_{on}} = C_S V^2_{\rm load}$. It is convenient to design the snubber capacitor C_S for $I_{\rm MP}$ at $\Delta T_{\rm max}$.

Next, these results are applied to the experimental case of Fig. 10, in which $\Delta T = 0.37\,\mu$s, $V_{\rm max} - V_{\rm load} = 18\,$V and $I_{\rm in}(t_{\rm on}) = 2.17\,$A. Using (11), L_P is estimated at 767 nH, hence using (15) the required snubber capacitor is 174 nF.

Fig. 11 shows the improvements to the TEG's transient response when adding a 220-nF ceramic capacitor (commercial value closest to 174 nF), during the same operating conditions. Also, two diodes, D_{S1} and D_{S2}, are used to add some damping due to their conduction resistances, and to provide a Schmitt trigger function because of their voltage drops. The resulting circuit is effectively a *diode capacitor diode (DCD) snubber*, which suppresses overvoltages storing energy during $t_{\rm off}$ and releasing it back during $t_{\rm on}$. Fig. 11 also includes results using the proposed DCD snubber circuit. The overvoltage is reduced from 18 to 1 V in both cases. Experimental and simulation results have proven that the settling time is shorter when the two diodes are used. By way of comparison, the settling time is reduced from 2.5 to 2.09 μs with the capacitor and to 1.48 μs with the proposed DCD snubber.

It is a design choice to use smaller values for the snubber capacitor in order to reach a compromise between speed of transient response and magnitude of overvoltage.

As an alternative, it would not be possible to use a transient voltage suppressor, because the open circuit voltage varies, therefore a constant breakdown voltage cannot be selected.

B. Synchronous Buck-Boost

A noninverting synchronous Buck-Boost was chosen because of its adaptability to working with a wide range of input voltages, smaller or greater than the output voltage, which is fixed by the battery voltage. The "common" noninverting synchronous Buck–Boost converter [49]–[52] uses four switches, however, to prevent the battery from discharging in case the converter runs in the discontinuous conduction mode, the output switch is in this work replaced by a Schottky diode.

A Microchip PIC16F microcontroller activates the gate drivers with two 180° anti-phase PWMs, running at 78 kHz. The microcontroller measures the TEG voltage at the converter's input and the battery's voltage V_b at the output. After measuring the open-circuit voltage $V_{\rm OC}$, the algorithm calculates the initial PWM's duty cycle using the ideal relation: $2V_b/V_{\rm OC} = D/(1-D)$. At every successive microcontroller's program iteration, the input voltage $V_{\rm in}$ is measured and a digital control loop keeps on adjusting the duty cycle to maintain $V_{\rm in} = V_{\rm OC}/2$. In this way, the converter minimizes parasitic effects and deals with changes in the battery voltage, e.g., load transients. The converter is intended to be used with the three TEG devices described in Section II, electrically connected in series, however it can be used with other TEGs with different *V–I* characteristics ($I_{\rm in,max} = 5$ A, $V_{\rm in,max} = 30$ V, $P_{\rm rated} = 35$ W). The three TEGs in series produce a maximum open-circuit voltage of 27 V and the MP is approximately 30.4 W at $V_{\rm MP} = 13.5$ V and $I_{\rm MP} = 2.25$ A. Fig. 12 shows the converter's PCB, which measures $75 \times 55\,{\rm mm}^2$. The n-MOSFETs used are IPD036N04L, the power Schottky is VS-12CWQ03FN, and the inductor is 15 μH ($I_{\rm sat} = 14$ A), the input capacitors are a total of 440 μF (50 V) and the output ones a total of 660 μF (25 V). Both input and output capacitors were chosen based on their RMS current capabilities. Using the electrical values at maximum available TEG power and with a battery voltage of 12 V, the maximum RMS current in the input capacitors is calculated from (6) to be 2.62 A.

The MP loss on $M_{\rm cap}$ is 21 mW (from (8), assuming an on-resistance of 3.6 mΩ). This corresponds to 10.5 mJ lost every 500 ms. As a comparison, with the "common" fractional open-circuit technique that waits for the input capacitors to charge up to open circuit through the TEG's internal resistance ($\sim 6\,\Omega$), the RC time constant is $\tau_{\rm RC} = 2.64$ ms. Waiting for $3\,\tau_{\rm RC}$ not harvesting 30 W equates to losing 237 mJ.

The converter's electrical efficiency was tested with a power supply in series with a fixed 6-Ω power resistor and the results are listed in Table III. The efficiency is 92.6% when tested at 30.4 W(13.5 V, 2.25 A) input. It must be noted that the MPPT technique presented in Section III can be used with any other similar type of converter.

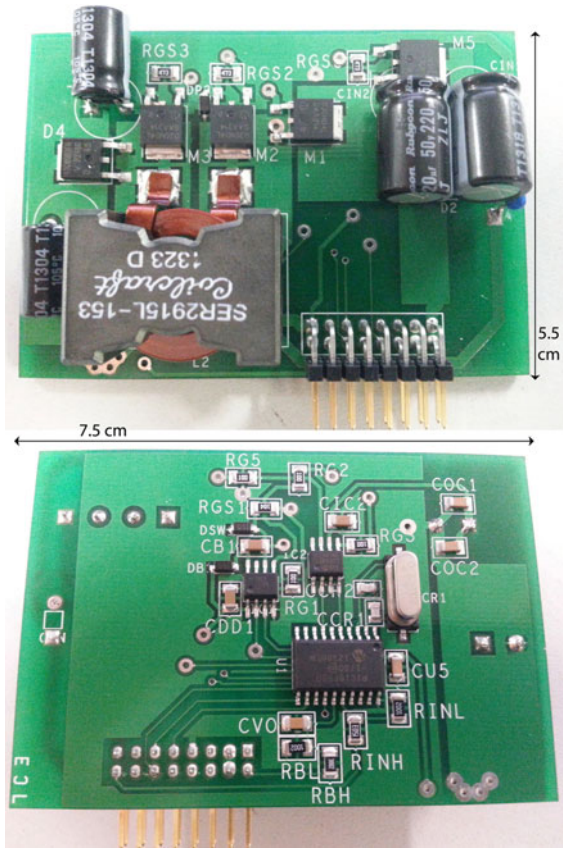

Fig. 12. Image of the PCB of the MPPT converter.

TABLE III
ELECTRICAL PERFORMANCE OF THE SYNCHRONOUS BUCK-BOOST TESTED WITH A POWER SUPPLY IN SERIES WITH A 6-Ω POWER RESISTOR

$V_{in}(V)$	$I_{in}(A)$	$P_{in}(W)$	$P_{out}(W)$	$\eta_{el}(\%)$
3	0.5	1.5	1.17	78.1
5	0.83	4.17	3.69	88.5
7.5	1.25	9.38	8.40	89.6
10.5	1.75	18.38	16.70	90.9
13.5	2.25	30.38	28.13	92.6

The $V_{\rm OC}$ measurement is performed every 500 ms and it lasts for eight switching cycles $T_{\rm sw}$, which corresponds to less than 110 μs. Considering a PWM duty cycle of 50%, the converter is disconnected from the TEGs for just 0.011% of the time.

Fig. 13 shows the converter's input voltage and current during the $V_{\rm OC}$ measurement. The converter is initially running at 13.35 V, 2.07 A at the input. After 45 μs $M_{\rm cap}$ is switched OFF therefore the input voltage goes to $V_{\rm OC}$, during $t_{\rm off}$, after an overshoot of less than 6 V when using a DCD snubber with 100-nF ceramic capacitor. The ADC measurement starts 2 μs after the PWM goes low. It can be noted that during $t_{\rm on}$ current is drawn from the TEGs and that during the $V_{\rm OC}$ measurement the voltage across the input capacitors decreases from 12.86 to 12.46 V as described by (10). The initial drop from 13.35 to 12.86 V is due to the voltage drop across the body diode of $M_{\rm cap}$.

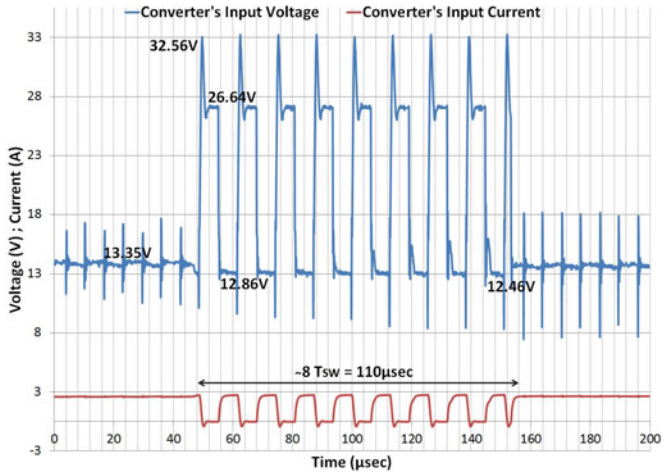

Fig. 13. Converter's input voltage and current during the measurement of the open-circuit voltage.

V. Experimental Results

The choice of using three TEGs is dictated by the need of testing the MPPT converter around its power rating and with a relatively high maximum TEG voltage. As explained in Section II-C not only are the performances of the three devices almost identical, but the mathematical characterization guarantees the estimation of performance relative to each independent TEG device.

Three experiments were designed to test the steady state and transient performance of the proposed MPPT converter. First, the steady-state performance is measured using TEGs. Next, a sudden $V_{\rm OC}$ transient is created by substituting the TEGs with a power supply in series with a power resistor. Finally, a thermal transient was created in the test rig to analyze the tracking performance of the MPPT converter during continuously changing thermal operating conditions.

The PCB used is not equipped with a current sensor, therefore it cannot be used for experimental comparison with other MPPT techniques. However, where possible the obtained performance are compared to results found in the literature. In all the experiments, a $12\,\mathrm{V}, 7\,Ah$ lead–acid battery is used to accumulate the power transferred through the converter. An electronic load was connected to prevent the battery from overcharging.

A. Steady-State Performance

The aim of this experiment is to compare the power extracted by the MPPT converter to the MP available from the three TEMs, maintained at the same temperature difference. Three separate tests have been undertaken, each one selecting a different thermal operating point, i.e., temperature gradient across the devices. The temperature gradients used are $\Delta T = 100\,^{\circ}\mathrm{C}, 150\,^{\circ}\mathrm{C}, 200\,^{\circ}\mathrm{C}$, which are the same used for the electrical characterization of the devices in Section II.

When the three modules are electrically connected in series, their open-circuit voltages and internal resistances sum so that the resulting array can still be represented by a voltage source in series with an internal resistance and the MPP remains at half

TABLE IV
Comparison of the Steady-State Tracking Performance of the MPPT Converter With the Maximum Available Power From the Series-Connected Array

	Exp Max Power		MPPT Converter		
ΔT ($^{\circ}C$)	I_{MP} (A)	P_{max} (W)	I_{MPPT} (A)	P_{MPPT} (W)	P_{var} (%)
100	1.38	10.09	1.33	10.07	0.15
150	1.84	19.88	1.84	19.89	0.00
200	2.17	30.06	2.09	30.02	0.14

$V_{\rm OC}$. The procedure to compare the electrical operating point set by the converter to the MPP is the following:

1) Confirm that the actual series open-circuit voltage corresponds to $V_{\mathrm{OC,S}} = V_{\mathrm{OC},1} + V_{\mathrm{OC},2} + V_{\mathrm{OC},3}$ from Table II.
2) Calculate the theoretical current for MP: $I_{\rm MP} = \frac{V_{\mathrm{OC,S}}}{2(R_1+R_2+R_3)}$
3) Calculate the theoretical MP: $P_{\rm max} = V_{\rm MP} I_{\rm MP} = \frac{V_{\mathrm{OC,S}}^2}{4(R_1+R_2+R_3)}$
4) Read the current $I_{\rm op}$ set by the MPPT converter
5) Use $I_{\rm op}$ to calculate the actual power produced by each of the three TEGs, using the individual "mathematical" formulation from (3) ($\pm 1.5\%$ accuracy).

It is important to note that it is not possible to sum the individual values of MP from Table II (and thus replace points 1 to 3) because those MPPs are relative to slightly different values of current, which it is not possible to have in a series array. As an alternative, it would also be possible to use the voltage reading from the multimeter or the oscilloscope, however this procedure is less precise due to the switching noise; the current reading is measured with both a multimeter and an oscilloscope probe.

The results of the steady-state test are summarized in Table IV. The last column shows that the MPPT converter has an accuracy, sometimes called *tracking efficiency*, of 99.85% (calculated with a maximum error of 1.5%). The fractional open-circuit voltage MPPT converter presented in [32] maintains the input voltage within 5% of $V_{\rm OC}/2$ except for small values of $V_{\rm OC}$. In [22], fractional short circuit and P&O are compared but the MPPT efficiency is not calculated. The INC MPPT control proposed in [30] shows a 95% tracking efficiency. The P&O MPPT converter of [29] is calculated to have around 99% tracking efficiency, but this is not accurately proved experimentally, as done in this paper.

B. Sudden-Transient Performance

This test allows characterizing the settling response of the converter after a step change in the open-circuit voltage. Such a test cannot be performed with real TEGs: it is impossible to instantaneously change their open-circuit voltage, therefore the TEGs have been replaced by a power supply in series with a power resistor of $4.7\,\Omega$. Fig. 14 shows the response of the MPPT converter after a $V_{\rm OC}$ step from 10 to 20 V. After measuring the open-circuit voltage for $110\,\mu$s (DCD snubber with 100-nF ceramic capacitor), the MPPT converter regulates the input voltage to half of $V_{\rm OC}$ in $8\,$ms. It can be noted that the input voltage starts at $5\,$V and ends at $10\,$V which correspond to

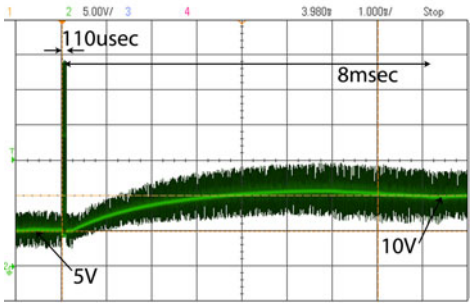

Fig. 14. Converter's input voltage after a V_{OC} step-up from 10 to 20 V. Time: 1 ms/div (x-axis); Voltage: 5 V/div (y-axis).

half of 10 V and 20 V, respectively, as expected. A similar test was undertaken in [30], demonstrating a 300 ms settling time.

C. TEG Transient Performance

The third experiment assesses the ability of the MPPT converter to respond to changes of the thermal input power, i.e., changes of the temperature gradient. In the test rig, the fastest thermal transient occurs during the cool down of the TEGs. The TEGs are initially maintained at 200 °C, then the power to the heaters is disconnected and the temperature difference diminishes at a rate of 0.25 °C/s due to the heat absorption capacity of the water cooling system. A datalogger records all the temperatures, while two multimeters measure the converter's input voltage and current. Both instruments are controlled by a VEE Pro program that records all the data in spreadsheet format.

The temperature differences across the three devices are not always exactly the same at any given instant, therefore the actual power extracted by the MPPT converter is compared to the theoretical MP available, as calculated for the steady-state experiment. This experiment is effectively a continuous series of steady-state experiments because the thermal time constant of the TEG system is much slower than the transient response of the converter, which adjusts the operating point every 0.5 s. The results (in blue) are shown in Fig. 15, where a $\pm 2\%$ margin has been added over the maximum available power (in red), to take into account the accuracy of the mathematical characterization and measurement errors. Considering each point, the average tracking efficiency of the MPPT converter is 98.7%. None of the MPPT converters for TEGs presented in the literature is tested with a TEG thermal transient. The test rig used cannot provide faster temperature transients, however it must be noted that due to how this MPPT algorithm is computed, without any integral term, the converter can track the MPP every 500 ms, even if this period could be simply reduced in the microcontroller's code. It has been selected based on practical experience about the thermal time constant of the TE system.

VI. Conclusion

This paper presented an innovative technique to obtain the open-circuit voltage measurement of a TEG, with minimal disconnection of the load. The MPPT algorithm is programmed to a low-cost microcontroller and does not require expensive

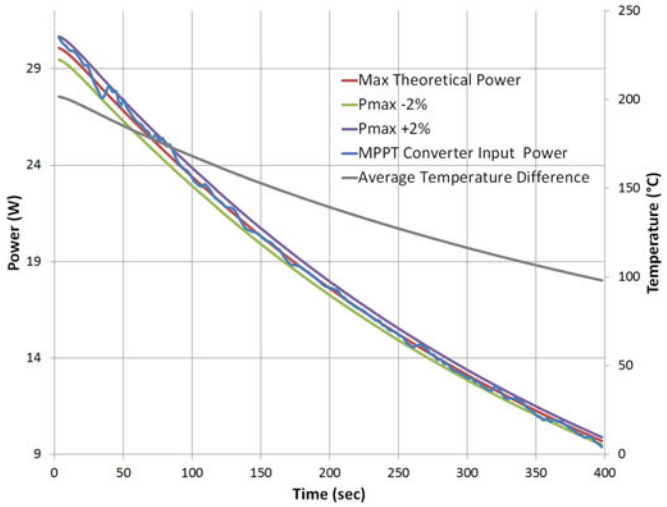

Fig. 15. Thermal transient from $\Delta T = 200$ °C to $\Delta T = 100$ °C across the three TEGs. Available and extracted output power on the left y-axis and temperature difference on the right y-axis.

sensors; it checks the open-circuit voltage every 500 ms and accurately adjusts the optimum operating point in less than 10 ms.

The converter used is a dc–dc noninverting synchronous Buck-Boost (93% efficient), which can work in Boost, Buck-Boost or Buck mode; this guarantees the harvest of power over a wide range of temperature differences across the TEG.

The presented MPPT system was tested both under steady state and transient conditions with real TEGs, demonstrating its ability to set the optimum electrical operating point quickly and very accurately. It is able to harvest close to 100% of the MP that can be produced by the TEG in the steady state and 98.7% during thermal transients. These results exceed the performance of any other MPPT algorithm for TEG applications presented in the literature so far.

Future work will focus on comparing the proposed MPPT technique to other MPPT algorithms, and on integrating several MPPT converters together to form a DMPPT system.

Acknowledgment

The authors would like to thank M. Compadre Torrecilla.

References

[1] D. Rowe, *Thermoelectrics Handbook: Macro to Nano*. Boca Raton, FL, USA: CRC Press, 2005.

[2] D. Rowe, "Thermoelectrics, an environmentally-friendly source of electrical power," *Renewable Energy*, vol. 16, pp. 1251–1256, 1999.

[3] D. Rowe, "Thermoelectric waste heat recovery as a renewable energy source," *Int. J. Innov. Energy Syst. Power*, vol. 1, no. 1, pp. 13–23, 2006.

[4] R. J. Mehta, Y. Zhang, C. Karthik, B. Singh, R. W. Siegel, T. Borca-Tasciuc, and G. Ramanath. (2012, Mar.). A new class of doped nanobulk high-figure-of-merit thermoelectrics by scalable bottom-up assembly. *Nature Mater.* [Online]. *11(3)*, pp. 233–240. Available: http://www.ncbi.nlm.nih.gov/pubmed/22231596

[5] K. Biswas, J. He, I. D. Blum, C.-I. Wu, T. P. Hogan, D. N. Seidman, V. P. Dravid, and M. G. Kanatzidis. (2012, Sep.). High-performance bulk thermoelectrics with all-scale hierarchical architectures. *Nature* [Online]. *489(7416)*, pp. 414–418. Available: http://www.nature.com/doifinder/10.1038/nature11439

[6] D. Crane, J. LaGrandeur, V. Jovovic, M. Ranalli, M. Adldinger, E. Poliquin, J. Dean, D. Kossakovski, B. Mazar, and C. Maranville. (2012, Nov.). TEG on-vehicle performance and model validation and what it means for further TEG development. *J. Electron. Mater.* [Online]. Available: http://www.springerlink.com/index/10.1007/s11664-012-2327-8

[7] S. Risse and H. Zellbeck, "Close-coupled exhaust gas energy recovery in a gasoline engine," *Res. Therm. Manag.*, vol. 74, pp. 54–61, 2013.

[8] R. Nuwayhid, A. Shihadeh, and N. Ghaddar. (2005, Jun.). Development and testing of a domestic woodstove thermoelectric generator with natural convection cooling. *Energy Convers. Manag.* [Online]. *46(9–10)*, pp. 1631–1643. Available: http://linkinghub.elsevier.com/retrieve/pii/S0196890404001931

[9] J. A. B. Vieira and A. M. Mota. (2009, Jul.). Thermoelectric generator using water gas heater energy for battery charging. in *Proc. IEEE Int. Conf. Control Appl.* [Online]. pp. 1477–1482. Available: http://ieeexplore.ieee.org/lpdocs/epic03/wrapper.htm?arnumber=5281185

[10] D. Champier, J. P. Bédécarrats, T. Kousksou, M. Rivaletto, F. Strub, and P. Pignolet. (2011, Mar.). Study of a TE (thermoelectric) generator incorporated in a multifunction wood stove. *Energy* [Online]. *36(3)*, pp. 1518–1526. Available: http://linkinghub.elsevier.com/retrieve/pii/S0360544211000132

[11] S. O'Shaughnessy, M. Deasy, C. Kinsella, J. Doyle, and A. Robinson. (2013, Feb.). Small scale electricity generation from a portable biomass cookstove: Prototype design and preliminary results. *Appl. Energy* [Online]. *102*, pp. 374–385. Available: http://linkinghub.elsevier.com/retrieve/pii/S0306261912005545

[12] C. Suter, Z. Jovanovic, and A. Steinfeld. (2012, Nov.). A 1kWe thermoelectric stack for geothermal power generation—Modeling and geometrical optimization. *Appl. Energy* [Online]. *99*, pp. 379–385. Available: http://linkinghub.elsevier.com/retrieve/pii/S0306261912004060

[13] T. Kyono, R. Suzuki, and K. Ono. (2003, Jun.). Conversion of unused heat energy to electricity by means of thermoelectric generation in condenser. *IEEE Trans. Energy Convers.* [Online]. *18(2)*, pp. 330–334. Available: http://ieeexplore.ieee.org/lpdocs/epic03/wrapper.htm?arnumber=1201107

[14] J. Siviter, A. Knox, J. Buckle, A. Montecucco, and M. Euan, "Megawatt scale energy recovery in the Rankine cycle," in *Proc. IEEE Energy Convers. Congr. Expo.*, 2012, pp. 1374–1379.

[15] Y. K. Ramadass and A. P. Chandrakasan. (2011, Jan.). A batteryless thermoelectric energy harvesting interface circuit with 35 mV startup voltage. *IEEE J. Solid-State Circuits* [Online]. *46(1)*, pp. 333–341. Available: http://ieeexplore.ieee.org/lpdocs/epic03/wrapper.htm?arnumber=5599946

[16] A. Elefsiniotis, M. Weiss, T. Becker, and U. Schmid. (2013, Feb.). Efficient power management for energy-autonomous wireless sensor nodes for aeronautical applications. *J. Electron. Mater.* [Online]. Available: http://link.springer.com/10.1007/s11664-012-2468-9

[17] J. Kim and C. Kim, "A DC–DC boost converter with variation-tolerant MPPT technique and efficient ZCS circuit for thermoelectric energy harvesting applications," *IEEE Trans. Power Electron.*, vol. 28, no. 8, pp. 3827–3833, Aug. 2013.

[18] W. Wang, V. Cionca, N. Wang, M. Hayes, B. O'Flynn, and C. O'Mathuna, "Thermoelectric energy harvesting for building energy management wireless sensor networks," *Int. J. Distrib. Sens. Netw.*, vol. 2013, art. ID 232438, 14 pp., 2013. Available: http://dx.doi.org/10.1155/2013/232438.

[19] A. Montecucco and A. R. Knox. (2014). Accurate simulation of thermoelectric power generating systems. *Appl. Energy* [Online]. *118*, pp. 166–172. Available: http://www.sciencedirect.com/science/article/pii/S0306261913010271

[20] G. Min and D. Rowe. (2002, Jan.). "Symbiotic" application of thermoelectric conversion for fluid preheating/power generation. *Energy Convers. Manag.* [Online]. *43(2)*, pp. 221–228. Available: http://linkinghub.elsevier.com/retrieve/pii/S0196890401000243

[21] A. Patyk. (2013, Feb.). Thermoelectric generators for efficiency improvement of power generation by motor generators—Environmental and economic perspectives. *Appl. Energy* [Online]. *102*, pp. 1448–1457. Available: http://linkinghub.elsevier.com/retrieve/pii/S0306261912006472

[22] I. Laird and D. D.-C. Lu, "High step-up DC/DC topology and MPPT algorithm for use with a thermoelectric generator," *IEEE Trans. Power Electron.*, vol. 28, no. 7, pp. 3147–3157, Jul. 2013.

[23] Y. Wang, C. Dai, and S. Wang. (2013, Dec.). Theoretical analysis of a thermoelectric generator using exhaust gas of vehicles as heat source. *Appl. Energy* [Online]. *112*, pp. 1171–1180. Available: http://linkinghub.elsevier.com/retrieve/pii/S0306261913000275

[24] A. Montecucco, J. Siviter, and A. R. Knox. (2014). The effect of temperature mismatch on thermoelectric generators electrically connected in series and parallel. *Appl. Energy* [Online]. *123*, pp. 47–54. Available: http://www.sciencedirect.com/science/article/pii/S0306261914001664

[25] R. C. N. Pilawa-Podgurski and D. J. Perreault, "Submodule integrated distributed maximum power point tracking for solar photovoltaic applications.," *IEEE Trans. Power Electron.*, vol. 28, no. 6, pp. 2957–2967, Jun. 2013.

[26] M. Vitelli. (2012, Jul.). On the necessity of joint adoption of both distributed maximum power point tracking and central maximum power point tracking in PV systems. *Progr. Photovoltaic, Res. Appl.* [Online]. Available: http://doi.wiley.com/10.1002/pip.2256

[27] L. Chen, D. Cao, H. Yi, and F. Z. Peng. (2008, Jun.). Modeling and power conditioning for thermoelectric generation. in *Proc. IEEE Power Electron. Spec. Conf.*, pp. 1098–1103. [Online]. Available: http://ieeexplore.ieee.org/lpdocs/epic03/wrapper.htm?arnumber=4592076

[28] R.-Y. Kim and J.-S. Lai, "A seamless mode transfer maximum power point tracking controller for thermoelectric generator applications.," *IEEE Trans. Power Electron.*, vol. 23, no. 5, pp. 2310–2318, Sep. 2008.

[29] D. Champier, C. Favarel, J. P. Bédécarrats, T. Kousksou, and J. F. Rozis. (2013, Jan.). Prototype combined heater/thermoelectric power generator for remote applications. *J. Electron. Mater.* [Online]. Available: http://link.springer.com/10.1007/s11664-012-2459-x

[30] R.-Y. Kim, J.-S. Lai, B. York, and A. Koran. (2009, Sep.). Analysis and design of maximum power point tracking scheme for thermoelectric battery energy storage system. *IEEE Trans. Ind. Electron.* [Online]. *56(9)*, pp. 3709–3716. Available: http://ieeexplore.ieee.org/lpdocs/epic03/wrapper.htm?arnumber=5130124

[31] H. Nagayoshi and T. Kajikawa. (2006). Mismatch power loss reduction on thermoelectric generator systems using maximum power point trackers. in *Proc. 25th Int. Conf. Thermoelectr.* [Online]. pp. 210–213. Available: http://ieeexplore.ieee.org/lpdocs/epic03/wrapper.htm?arnumber=4133272

[32] D. E. Schwartz. (2012, Jun.). A maximum-power-point-tracking control system for thermoelectric generators. in *Proc. 3rd IEEE Int. Symp. Power Electron. Distrib. Generation Syst.* [Online], pp. 78–81. Available: http://ieeexplore.ieee.org/lpdocs/epic03/wrapper.htm?arnumber=6253982

[33] I. Laird, H. Lovatt, N. Savvides, D. Lu, and V. G. Agelidis, "Comparative study of maximum power point tracking algorithms for thermoelectric generators," in *Proc. Australas. Univ. Power Eng. Conf.*, 2008, pp. 1–6.

[34] A. Montecucco, J. R. Buckle, and A. R. Knox. (2012, Mar.). Solution to the 1-D unsteady heat conduction equation with internal Joule heat generation for thermoelectric devices. *Appl. Therm. Eng.* [Online]. *35*, pp. 177–184. Available: http://linkinghub.elsevier.com/retrieve/pii/S1359431111005643

[35] D. Rowe and G. Min. (1998, Jun.). Evaluation of thermoelectric modules for power generation. *J. Power Sources* [Online]. *73(2)*, pp. 193–198. Available: http://linkinghub.elsevier.com/retrieve/pii/S0378775397028012

[36] S. Lineykin and S. Ben-Yaakov. (2007). Modeling and analysis of thermoelectric modules. *IEEE Trans. Ind. Appl.* [Online]. *43(2)*, pp. 505–512. Available: http://ieeexplore.ieee.org/lpdocs/epic03/wrapper.htm?arnumber=4132878

[37] S. Chiwanga, K. Simpson, R. Gilchrist, and A. Montecucco, "Characterization of commercial thermoelectric module using experimental and numerical techniques to compile performance data," in *Proc. 3rd Conf. Thermoelectr.*, 2012.

[38] A. Samarelli, L. F. Llin, S. Cecchi, J. Frigerio, T. Etzelstorfer, E. Muller, Y. Zhang, J. R. Watling, D. Chrastina, G. Isella, J. Stangl, J. P. Hague, J. M. R. Weaver, P. Dobson, and D. J. Paul. (2013). The thermoelectric properties of Ge/SiGe modulation doped superlattices. *J. Appl. Phys.* [Online]. *113(23)*, pp. 233704-1–233704-13. Available: http://link.aip.org/link/JAPIAU/v113/i23/p233704/s1&Agg=doi

[39] M. Brignone and A. Ziggiotti. (2011). Impact of novel thermoelectric materials on automotive applications. in *Proc. 9th Eur. Conf. Thermoelectr.* [Online]. pp. 493–496. Available: http://link.aip.org/link/APCPCS/v1449/i1/p493/s1&Agg=doi

[40] J. W. Fergus. (2012, Mar.). Oxide materials for high temperature thermoelectric energy conversion. *J. Eur. Ceram. Soc.* [Online]. *32(3)*, pp. 525–540. Available: http://linkinghub.elsevier.com/retrieve/pii/S0955221911005036

[41] L. Ferre Llin, A. Samarelli, S. Cecchi, T. Etzelstorfer, E. Muller Gubler, D. Chrastina, G. Isella, J. Stangl, J. M. R. Weaver, P. S. Dobson, and D. J. Paul. (2013). The cross-plane thermoelectric properties of p-Ge/Si0.5Ge0.5 superlattices. *Appl. Phys. Lett.*

[Online]. *103(14)*, pp. 143507-1–143507-4. Available: http://link.aip.org/link/APPLAB/v103/i14/p143507/s1&Agg=doi

[42] A. Montecucco, J. Buckle, J. Siviter, and A. R. Knox. (2013, Mar.). A new test rig for accurate nonparametric measurement and characterization of thermoelectric generators. *J. Electron. Mater.*. [Online]. Available: http://link.springer.com/10.1007/s11664-013-2484-4

[43] B. C. Woo, D. Y. Lee, H. W. Lee, and K. I. J., "Characteristic of maximum power with temperature difference for thermoelectric generator," in *Proc. 20th Int. Conf. Thermoelectr.*, 2001, pp. 431–434.

[44] J. Chen, Z. Yan, and L. Wu. (1996). The influence of Thomson effect on the maximum power output and maximum efficiency of a thermoelectric generator. *J. Appl. Phys.* [Online]. *79(11)*, pp. 8823–8828. Available: http://link.aip.org/link/JAPIAU/v79/i11/p8823/s1&Agg=doi

[45] A. Montecucco, J. Siviter, and A. R. Knox, "Simple, fast and accurate maximum power point tracking converter for thermoelectric generators," in *Proc. IEEE Energy Convers. Congr. Expo.*, 2012, pp. 2777–2783.

[46] J. Gao and M. Chen. (2013, Oct.). Beat the deviations in estimating maximum power of thermoelectric modules. *IEEE Trans. Instrum. Meas.* [Online]. *62(10)*, pp. 2725–2729. Available: http://ieeexplore.ieee.org/lpdocs/epic03/wrapper.htm?arnumber=6568931

[47] C. Basso, *Switch-Mode Power Supplies: Spice Simulations and Practical Designs*. New York, NY, USA: McGraw-Hill, 2008.

[48] R. W. Erickson and D. Maksimović, *Fundamentals of Power Electronics*. New York, NY, USA: Springer-Verlag, 2001.

[49] B. Sahu and G. Rincon-Mora. (2004, Mar.). A low voltage, dynamic, noninverting, synchronous buck-boost converter for portable applications. *IEEE Trans. Power Electron.* [Online]. *19(2)*, pp. 443–452. Available: http://ieeexplore.ieee.org/lpdocs/epic03/wrapper.htm?arnumber=1271328

[50] J.-K. Shiau, C.-j. Cheng, and C.-E. Tseng. (2008, Nov.). Stability analysis of a non-inverting synchronous buck-boost power converter for a solar power management system. in *Proc. IEEE Int. Conf. Sustainable Energy Technol.* [Online]. pp. 263–268. Available: http://ieeexplore.ieee.org/lpdocs/epic03/wrapper.htm?arnumber=4747014

[51] M. Orellana, S. Petibon, B. Estibals, and C. Alonso. (2010, Nov.). Four switch buck-boost converter for photovoltaic DC–DC power applications. in *Proc. 36th Annu. Conf. IEEE Ind. Electron. Soc.* [Online]. no. 1, pp. 469–474. [Online]. Available: http://ieeexplore.ieee.org/lpdocs/epic03/wrapper.htm?arnumber=5674983

[52] J.-J. Chen, P.-N. Shen, and Y.-S. Hwang, "A high-efficiency positive buck-boost converter with mode-select circuit and feed-forward techniques," *IEEE Trans. Power Electron.*, vol. 28, no. 9, pp. 4240–4247, Sep. 2013.

Andrea Montecucco (S'10) received the B.Sc. and M.Sc. degrees from the University of Padova, Padua, Italy, in 2007 and 2009, and he is currently working toward the Ph.D. degree at the University of Glasgow, Glasgow, U.K.

He has previously been Research Assistant for two years at the University of Glasgow. He has authored more than ten papers in journals and at professional conferences, and holds one International patent. His research interests include analog and embedded electronics design, testing and simulation of thermoelectric systems, maximum power and maximum efficiency tracking for thermoelectric generators, solar cells and solar thermal, and dc–dc power converters.

Andrew R. Knox (SM'00) received the B.Sc. and Ph.D. degrees from the University of Glasgow, Glasgow, U.K., in 1985 and 2000, respectively.

He is currently a Professor of Power Electronics and Renewable Energy Systems at the University of Glasgow. He is also a Director of the Energy Technology Partnership and a Member of the National Physical Laboratory Advisory Board. Previously, he held senior managerial and technical positions in IBM Manufacturing, R&D for more than 22 years, working on Hi-Res displays, advanced graphics, electronic security, and PC architectures. He has published more than 40 papers, coauthored a book, contributed to International Standards, and holds more than 50 patents. His current research interests include analog and embedded electronics, thermoelectric, PV and solar thermal systems design, and smart grids.